Fully anharmonic nonperturbative theory of vibronically renormalized electronic band structures

Marios Zacharias,* Matthias Scheffler, and Christian Carbogno†
NOMAD Laboratory, Fritz Haber Institute, Faradayweg 4-6, 14195 Berlin Germany

(Received 23 March 2020; revised 22 June 2020; accepted 23 June 2020; published 20 July 2020)

We develop a first-principles approach for the treatment of vibronic interactions in solids that overcomes the main limitations of state-of-the-art electron-phonon coupling formalisms. In particular, anharmonic effects in the nuclear dynamics are accounted for to all orders via *ab initio* molecular dynamics simulations. This nonperturbative, self-consistent approach evaluates the response of the wave functions along the computed anharmonic trajectory; thus, it fully considers the coupling between nuclear and electronic degrees of freedom. We validate and demonstrate the merits of the concept by calculating temperature-dependent, momentum-resolved spectral functions for silicon and the cubic perovskite $SrTiO_3$, a strongly anharmonic material featuring soft modes. In the latter case, our approach reveals that anharmonicity and higher-order vibronic couplings contribute substantially to the electronic structure at finite temperatures, noticeably affecting band gaps and effective masses and hence macroscopic properties such as transport coefficients.

DOI: 10.1103/PhysRevB.102.045126

I. INTRODUCTION

Electronic band structures are a fundamental concept in material science used to qualitatively understand and quantitatively assess optical and electronic properties of materials, e.g., charge carrier mobilities and absorption spectra of semiconductors. Over the last decade, three pivotal advancements have paved the way towards predictive, quantitative *ab initio* calculations of electronic band structures: Advances in relativistic approaches [1], improvements in the treatment of electronic exchange and correlation [2,3], and the inclusion of electron-phonon interactions via perturbative many-body formalisms based on the Allen-Heine theory [4]. The latter approach has been widely used to calculate temperature-dependent effects on the electronic structure stemming from nuclear motion [5–19]. However, such perturbative calculations rely on *two* approximations. (a) The nuclear motion is approximated in a harmonic model which is equivalent to the concept of phonons, and (b) the vibronic interaction between electronic and nuclear degrees of freedom is treated by perturbation theory in terms of electron-phonon coupling. In both approximations, interactions at finite temperatures T are thus described via truncated Taylor expansions, using derivatives computed at the static equilibrium geometry, i.e., for the total energy minimum corresponding to the atomic geometry $\boldsymbol{R}^{\mathrm{eq}}$ obtained in the classical $T = 0\,\mathrm{K}$ limit. Clearly, both these approximations are problematic whenever large deviations from $\boldsymbol{R}^{\mathrm{eq}}$ occur, e.g., at elevated temperatures and for soft bonded atoms. Several strategies have been proposed to mitigate either one of these approximations [20–28]. This revealed that the predictive power of perturbative calculations can be problematically limited, even for low-temperature properties of simple materials such as MgO and LiF [22]; solids featuring more anharmonic dynamics, such as molecular crystals [29]; and perovskites [30], which are affected more severely. A consistent computational approach able to settle these issues by accounting, on equal footing, for *both* anharmonic effects in the nuclear motion and the full vibronic coupling is, however, still lacking.

In this work, we fill this gap by deriving a fully anharmonic, nonperturbative first-principles theory of vibronic coupling and demonstrate its implementation in the all-electron, numeric atomic orbitals code FHI-AIMS [31]. As validation, we show that our approach reproduces literature data for Si, a largely harmonic case in which the perturbative approach works exceptionally well. Furthermore, we compute temperature-dependent spectral functions, band gaps, and effective masses for cubic $SrTiO_3$, a prototypical perovskite. In this case, the highly anharmonic dynamics [32,33] associated with the octahedral tilting typically observed in perovskites [34,35] results in a breakdown of the perturbative model and thus in significant changes in the electronic properties. Besides clarifying the experimental findings for $SrTiO_3$ [36,37], our calculations reveal that anharmonic, higher-order vibronic couplings (AVICs) have substantial influence on electronic properties, especially of perovskites, a material class with exceptional potential for high-temperature applications [38–43].

The organization of this paper is as follows: In Sec. II we introduce the theoretical framework of our statistically anharmonic, higher-order vibronic coupling (stAVIC) approach for obtaining full anharmonic temperature-dependent band structures. In the same section we also outline the main

*zachariasmarios@gmail.com
†carbogno@fhi-berlin.mpg.de

equations involved in our implementation of band structure unfolding using numeric atom-centered orbitals. In Sec. III we present all computational details of the calculations performed in this work. In Sec. IV we demonstrate the merits of our methodology by reporting first-principles calculations of temperature-dependent spectral functions and band gaps of Si and $SrTiO_3$ for a wide range of temperatures. For $SrTiO_3$, we also report temperature-dependent effective masses. Section V summarizes our key results and emphasizes the importance of our methodology for materials' design in various applications. Further technical details are left to Appendixes A–C.

II. THEORY

In this section we describe the theoretical framework of our methodology and discuss the implementation details of the band structure unfolding technique when numeric atom-centered orbitals are used.

A. Statistically anharmonic, higher-order vibronic coupling approach

In the following, the energy $\epsilon_l^{\boldsymbol{R}}$ of the electronic state $|\psi_l^{\boldsymbol{R}}\rangle$ is obtained by solving the Schrödinger equation $H_{\rm el}^{\boldsymbol{R}}|\psi_l^{\boldsymbol{R}}\rangle = \epsilon_l^{\boldsymbol{R}}|\psi_l^{\boldsymbol{R}}\rangle$, where $H_{\rm el}^{\boldsymbol{R}}$ is the electronic Hamiltonian of the system at the atomic geometry $\boldsymbol{R}$. This may be a Kohn-Sham Hamiltonian with a certain exchange-correlation functional. For readability, we use the generalized index l to indicate both the band index n and the wave vector $\boldsymbol{k}$. The temperature dependence of $\epsilon_l^{\boldsymbol{R}}$ is evaluated within the Born-Oppenheimer approximation via the canonical ensemble average at temperature T:

$$\langle\epsilon_l^{\boldsymbol{R}}\rangle_T = \frac{1}{Z}\int d\boldsymbol{R}d\boldsymbol{P}\exp\left[\frac{-E(\boldsymbol{R},\boldsymbol{P})}{k_{\rm B}T}\right]\epsilon_l^{\boldsymbol{R}}. \tag{1}$$

Here, $k_{\rm B}$ is the Boltzmann constant, Z is the canonical partition function, $\boldsymbol{P}$ is the momenta of the nuclei, and $E(\boldsymbol{R},\boldsymbol{P})$ is the total energy of the combined electronic and nuclear system. For the evaluation of Eq. (1), the state-of-the-art formalism [44] resorts to the *two* perturbative approximations mentioned above. When the harmonic approximation is employed for the potential-energy surface (PES) the classical equations of motions for $\boldsymbol{R},\boldsymbol{P}$ can be solved analytically, and so can the quantum-mechanical Schrödinger equation. Hence, Eq. (1) is approximated via $\langle\epsilon_l^{\boldsymbol{R}}\rangle_T \approx \langle\epsilon_l^{\boldsymbol{R}}\rangle_T^{\rm ha}$ as

$$\langle\epsilon_l^{\boldsymbol{R}}\rangle_T^{\rm ha} = \frac{1}{Z^{\rm ha}}\int d\boldsymbol{R}^{\rm ha}d\boldsymbol{P}^{\rm ha}\exp\left[\frac{-E^{\rm ha}(\boldsymbol{R}^{\rm ha},\boldsymbol{P}^{\rm ha})}{k_{\rm B}T}\right]\epsilon_l^{\boldsymbol{R}}, \tag{2}$$

which allows for a straightforward evaluation of the phase-space integral [24–26,45,46]. When the dependence of the electronic states on the nuclear motion is truncated up to second order in the atomic displacements $\epsilon_l^{\boldsymbol{R}} \approx \epsilon_l^{{\rm pt},\boldsymbol{R}}$, then the ensemble average in Eq. (2) yields the perturbative Allen-Heine energies $\langle\epsilon_l^{{\rm pt},\boldsymbol{R}}\rangle_T^{\rm ha}$.

In this work, we rely on neither of the two approximations. First, *ab initio* molecular dynamics (aiMD) trajectories with length t_0 are used to evaluate the canonical ensemble average in Eq. (1) as a time t average,

$$\langle\epsilon_l^{\boldsymbol{R}}\rangle_T = \langle\epsilon_l^{\boldsymbol{R}}\rangle_T^{\rm MD} = \lim_{t_0\to\infty}\frac{1}{t_0}\int_0^{t_0}\epsilon_l^{\boldsymbol{R}(t)}dt. \tag{3}$$

This accounts for the full anharmonicity of the PES. Second, the dependence of the electronic eigenenergies $\epsilon_l^{\boldsymbol{R}(t)}$ on the nuclear positions is explicitly evaluated by solving $H_{\rm el}^{\boldsymbol{R}(t)}|\psi_l^{\boldsymbol{R}(t)}\rangle = \epsilon_l^{\boldsymbol{R}(t)}|\psi_l^{\boldsymbol{R}(t)}\rangle$ at each aiMD step $\boldsymbol{R}(t)$. All orders of coupling between electronic and nuclear degrees of freedom are included by these means. This involves reexpanding

$$\left|\psi_l^{\boldsymbol{R}(t)}\right\rangle = \sum_m p_{ml}^{\boldsymbol{R}(t)}\left|\psi_m^{\rm eq}\right\rangle, \quad p_{ml}^{\boldsymbol{R}(t)} = \left\langle\psi_m^{\rm eq}\middle|\psi_l^{\boldsymbol{R}(t)}\right\rangle, \tag{4}$$

in terms of the wave functions at equilibrium $|\psi_m^{\rm eq}\rangle$. With that, one obtains

$$\epsilon_l^{\boldsymbol{R}(t)} = \left\langle\psi_l^{\boldsymbol{R}(t)}\middle|H_{\rm el}^{\boldsymbol{R}(t)}\middle|\psi_l^{\boldsymbol{R}(t)}\right\rangle = \epsilon_l^{\rm eq} + \sum_{m,n}\left[p_{nl}^{\boldsymbol{R}(t)}\right]^* p_{ml}^{\boldsymbol{R}(t)}\left\langle\psi_n^{\rm eq}\middle|H_{\rm el}^{\boldsymbol{R}(t)} - H_{\rm el}^{\rm eq}\middle|\psi_m^{\rm eq}\right\rangle. \tag{5}$$

In this form, it is evident that Eq. (5) incorporates not only the first nonvanishing derivatives of $H_{\rm el}^{\boldsymbol{R}(t)} - H_{\rm el}^{\rm eq}$ as perturbative formalisms but all orders. Similarly, all orders of couplings with the nuclear motion—not just quadratic terms—are captured via the coefficients $p_{ml}^{\boldsymbol{R}(t)}$, which describe the intricate $\boldsymbol{R}(t)$ dependence of the wave functions along the aiMD. Accordingly, all orders of AVIC are *statistically* captured by these means. Our approach, named stAVIC in the following, is thus valid even when the (harmonic) phonon ansatz is inappropriate.

In practice, the thermodynamic average in Eq. (3) can be evaluated via *ab initio* path-integral MD [47] or via aiMD [48], the latter corresponding to the classical, high-temperature limit of interest in this work. Regardless, a direct evaluation of Eq. (3) is not particularly useful since it does not give access to state- and momentum-resolved band structures in the fundamental Brillouin zone (BZ). Since large supercells are required to capture vibrations with a nonzero wave vector in solids, the obtained electronic energies $\epsilon_l = \epsilon_{N\boldsymbol{K}}^{\boldsymbol{R}(t)}$ and wave functions $\psi_l = \psi_{N\boldsymbol{K}}^{\boldsymbol{R}(t)}$, with band indices N and wave vectors $\boldsymbol{K}$, span only a reduced BZ [49] (capital letters indicate supercell quantities). As shown in Sec. II B, individual states thus become indistinguishable, and only band edges can be reliably identified [47,48]. Besides preventing a comparison with angle-resolved photoemission spectroscopy experiments or with the static limit at $\boldsymbol{R}^{\rm eq}$, for which the wave vectors $\boldsymbol{k}$ of $\epsilon_l^{\rm eq} = \epsilon_{n\boldsymbol{k}}^{\rm eq}$ and $\psi_l^{\rm eq} = \psi_{n\boldsymbol{k}}^{\rm eq}$ span the full fundamental BZ, this "BZ folding" makes it impossible to determine state- and momentum-dependent electronic properties, such as lifetimes and effective masses. To recover a band structure in the fundamental BZ also for supercells, the expansion coefficients introduced in Eq. (4) are used to "unfold" the states $\psi_{N\boldsymbol{K}}$. To this aim, we consider the spectral function expressed in the Lehman representation [50]:

$$A_{n\mathbf{k}}^{\boldsymbol{R}(t)}(E) = \sum_{N\mathbf{K}}\left|p_{n\mathbf{k},N\boldsymbol{K}}^{\boldsymbol{R}(t)}\right|^2\delta\left(E - \epsilon_{N\mathbf{K}}^{\boldsymbol{R}(t)}\right). \tag{6}$$

Compared to Eqs. (4) and (5), in which the perturbed eigenvalue $\epsilon_{N\mathbf{K}}^{\boldsymbol{R}(t)}$ is obtained from a superposition of equilibrium states $\psi_{n\mathbf{k}}^{\rm eq}$, Eq. (6) reflects the inverse relationship: Each perturbed eigenvalue $\epsilon_{N\mathbf{K}}^{\boldsymbol{R}(t)}$ contributes to all states $n\boldsymbol{k}$ in the

fundamental BZ, whereby $p^{\boldsymbol{R}(t)}_{n\boldsymbol{k},N\boldsymbol{K}} = \langle \psi^{\rm eq}_{n\mathbf{k}} | \psi^{\boldsymbol{R}(t)}_{N\mathbf{K}} \rangle$ determines the strength of this contribution.

For each configuration $\boldsymbol{R}(t)$, we obtain the momentum-resolved spectral function $A^{\boldsymbol{R}(t)}_{\mathbf{k}}(E) = \sum_n A^{\boldsymbol{R}(t)}_{n\mathbf{k}}(E)$ by summing over n in Eq. (6):

$$A^{\boldsymbol{R}(t)}_{\mathbf{k}}(E) = \sum_{N\mathbf{K}} P^{\boldsymbol{R}(t)}_{\mathbf{k},N\mathbf{K}} \delta\big(E - \epsilon^{\boldsymbol{R}(t)}_{N\mathbf{K}}\big). \tag{7}$$

The spectral weight $P^{\boldsymbol{R}(t)}_{\mathbf{k},N\mathbf{K}} = \sum_n |p^{\boldsymbol{R}(t)}_{n\boldsymbol{k},N\boldsymbol{K}}|^2$ describes the overlap between the supercell state $|\psi^{\boldsymbol{R}(t)}_{N\mathbf{K}}\rangle$ and all equilibrium states with wave vector $\mathbf{k}$ [51,52]. Details for its numerical evaluation are provided in Sec. II B. The momentum-resolved spectral function in thermodynamic equilibrium $\langle A^{\boldsymbol{R}(t)}_{\mathbf{k}}(E)\rangle_T$ is then computed as the thermodynamic average of $A^{\boldsymbol{R}(t)}_{\mathbf{k}}(E)$ along $\boldsymbol{R}(t)$ via Eq. (3). Momentum-resolved quasiparticle peaks are extracted from $\langle A^{\boldsymbol{R}(t)}_{\mathbf{k}}(E)\rangle_T$ by scanning over the energy axis, from which band gaps $\langle \epsilon_{\rm g}\rangle_T$ and effective masses m^*_e are then obtained.

B. stAVIC: Spectral weight formalism

In *ab initio* MD simulations of solids, it is necessary to use extended supercells to accurately sample vibrations with a nonzero wave vector. Due to the larger cell size in real space, the electronic structure obtained in reciprocal space from such supercell calculation suffers from BZ folding. In other words, the band structure is associated with a reduced BZ, as shown in Fig. 1(a). At finite temperatures, the motion of the nuclei breaks the symmetries within the supercell, thus making individual states indistinguishable [see Figs. 1(b) and 1(c)]. This prevents any assessment of the momentum dependence of the electronic dispersion. Hence, a BZ unfolding [49] is necessary to reverse this BZ folding and thus to obtain clearly disentangled states in the fundamental BZ and to map the properties of the dynamical system back onto the established language and terms of solid-state physics.

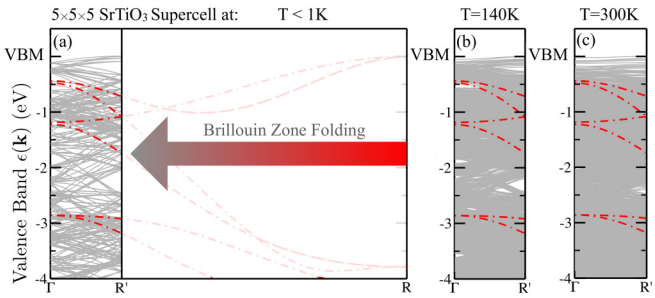

FIG. 1. Electronic valence band structure of $SrTiO_3$ along Γ-R obtained from calculations in the primitive unit cell with static nuclei at equilibrium (red) and in $5 \times 5 \times 5$ supercells (gray). As (a) exemplifies, the electronic dispersion $\epsilon(\boldsymbol{k})$ obtained in the primitive unit cell along Γ-R is "folded" into a reduced Brillouin zone with a shorter reciprocal-space path Γ-R' in supercell calculations. While individual states and their momentum dependence are still visible in the case of tiny displacements [(a), $T < 1$K], this is no longer the case at finite temperatures since the nuclear motion breaks the symmetries within the supercell. Accordingly, momentum-resolved electronic structures are no longer accessible, as (b) and (c) show for representative geometries obtained from aiMD runs at 140 and 300K, respectively.

The band-resolved spectral function $A_{n\mathbf{k}}(E)$ can be obtained from the imaginary part of the retarded one-electron Green's function [53] and then evaluated using Eq. (6). In practice, the electronic states are expanded [31] as a linear combination of Bloch-type functions using the expansion coefficients $c_{j,n\mathbf{k}}$ and $C_{J,N\mathbf{K}}$, respectively,

$$\psi_{n\mathbf{k}} = \sum_j c_{j,n\mathbf{k}}\, \chi_{j,\mathbf{k}}, \quad \psi_{N\mathbf{K}} = \sum_J C_{J,N\mathbf{K}}\, \chi_{J,\mathbf{K}}\,. \tag{8}$$

For notational clarity we have dropped the superscript indices eq and $\mathbf{R}(t)$ from the reference $\psi_{n\mathbf{k}}$ and perturbed $\psi_{N\mathbf{K}}$ states, respectively. The Bloch-type functions are related to atomic orbitals via discrete Fourier transforms

$$\chi_{j,\mathbf{k}} = \sum_{\boldsymbol{l}} e^{-i\mathbf{k}\cdot\boldsymbol{l}} \phi_{j,\boldsymbol{l}}, \tag{9}$$

$$\chi_{J,\mathbf{K}} = \sum_{\boldsymbol{L}} e^{-i\mathbf{K}\cdot\boldsymbol{L}} \Phi_{J,\boldsymbol{L}}, \tag{10}$$

in which the sums are taken over all lattice vectors $\boldsymbol{l} = (l_1, l_2, l_3)$ and $\boldsymbol{L} = (L_1, L_2, L_3)$. Enforcing translational invariance yields the overlap matrix elements $p_{n\boldsymbol{k},N\boldsymbol{K}}$ in the following form [54,55]:

$$\begin{aligned} p_{n\boldsymbol{k},N\boldsymbol{K}} &= \langle \psi_{n\mathbf{k}} | \psi_{N\mathbf{K}} \rangle \\ &= \sqrt{\frac{L}{l}} \sum_{jJ} c^*_{j,n\mathbf{k}} C_{J,N\mathbf{K}} \\ &\quad \times \sum_{\boldsymbol{l}} e^{-i\mathbf{k}\cdot\boldsymbol{l}}\, \langle \phi_{j,\boldsymbol{l}} | \Phi_{J,\mathbf{0}} \rangle\, \delta_{\mathbf{k}-\mathbf{G},\mathbf{K}}. \end{aligned} \tag{11}$$

Here, the first summation runs over all real basis functions $|\phi_{i,\boldsymbol{l}}\rangle$ and $|\Phi_{J,\mathbf{0}}\rangle$ of the reference and perturbed systems, respectively. The corresponding Born–von Karman supercells contain l and L periodic replicas of the original cell, set at $\mathbf{0}$, along each Cartesian direction. The presence of the Kronecker delta $\delta_{\mathbf{k}-\mathbf{G},\mathbf{K}}$ ensures that $\mathbf{K}$ is mapped onto $\mathbf{k}$ via a reciprocal lattice vector $\mathbf{G}$ of the perturbed system. For the mapping between the indices of the basis functions of the reference and perturbed system, j and J, the following relationship is satisfied:

$$\sum_{j'} s^{-1}_{jj'}(\mathbf{k}) S_{j'J}(\mathbf{K}) = \delta_{jJ}, \tag{12}$$

with

$$s_{jj'}(\mathbf{k}) = \sum_{\boldsymbol{l}} e^{i\mathbf{k}\cdot\boldsymbol{l}}\, \langle \phi_{j,\mathbf{0}} | \phi_{j',\boldsymbol{l}} \rangle\,, \tag{13}$$

$$S_{j'J}(\mathbf{K}) = \sqrt{\frac{L}{l}} \sum_{\boldsymbol{l}} e^{-i\mathbf{k}\cdot\boldsymbol{l}}\, \langle \phi_{j',\boldsymbol{l}} | \Phi^0_{J,\mathbf{0}} \rangle\, \delta_{\mathbf{k}-\mathbf{G},\mathbf{K}}. \tag{14}$$

Here, $|\Phi^0_{J,\mathbf{0}}\rangle$ indicates the basis functions of an unperturbed supercell, in which the atomic nuclei are at their equilibrium positions. In other words, $|\Phi^0_{J,\mathbf{0}}\rangle$ are the equilibrium states in the supercell, obtained by periodically replicating the unperturbed reference system. Taking the summation over all bands n in Eq. (11) yields the spectral weights $P_{\mathbf{k},N\mathbf{K}}$ entering Eq. (7). In particular, using the completeness relation $\mathbb{I}_{\mathbf{k}} =$

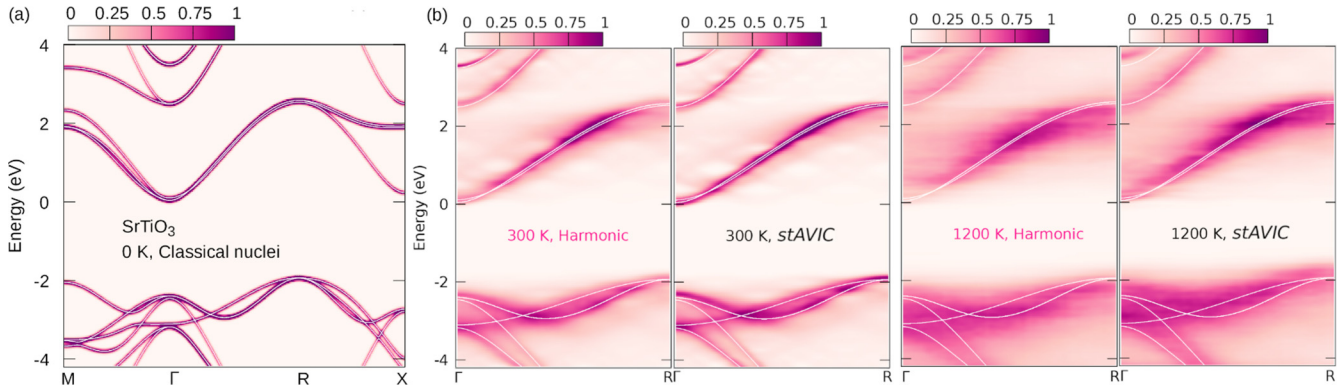

FIG. 2. (a) Spectral function $A_{\mathbf{k}}(E)$ of cubic $SrTiO_3$ along the high-symmetry path M-Γ-R-X (336 **k** points) calculated using DFT-PBE in a $5 \times 5 \times 5$ supercell containing 625 atoms at their classical, 0 K positions (static equilibrium). (b) Thermodynamically averaged spectral functions $\langle A_{\mathbf{k}}^{\mathbf{R}(t)}(E)\rangle_T$ of cubic $SrTiO_3$ along Γ-R (128 **k** points) for $T = 300$ and 1200 K calculated nonperturbatively on the harmonic and anharmonic PES using DFT-PBE and 30 uncorrelated geometries in a $5 \times 5 \times 5$ supercell containing 625 atoms. For all plots the band structure in static equilibrium is shown as white lines.

$\sum_n |\psi_{n\mathbf{k}}\rangle \langle\psi_{n\mathbf{k}}|$ of the states $|\psi_{n\mathbf{k}}\rangle$, the spectral weight can be rewritten as

$$P_{\mathbf{k},N\mathbf{K}} = \langle \Psi_{N\mathbf{K}} | \mathbb{I}_{\mathbf{k}} | \Psi_{N\mathbf{K}} \rangle \,, \tag{15}$$

and the final result with respect to the perturbed expansion coefficients and overlap matrix of the perturbed basis functions is

$$P_{\mathbf{k},N\mathbf{K}} = \frac{L}{l} \sum_{jJl} C^*_{J,N\mathbf{K}} C_{j,N\mathbf{K}} e^{-i\mathbf{k}\cdot\boldsymbol{l}} \langle \Phi_{j,\boldsymbol{l}} | \Phi_{J,\mathbf{0}} \rangle \, \delta_{\mathbf{k}-\mathbf{G},\mathbf{K}}. \tag{16}$$

The advantage of the above expression for the calculation of the spectral weights is that no knowledge of the wave functions of the reference system is explicitly required.

In our implementation we evaluate Eq. (7) by calculating the spectral weights using Eq. (16) and ensuring that the correct mapping between the j and J indices is obtained through Eq. (12). In Fig. 2(a) we demonstrate the first step of the validation of our approach by showing the perfect band structure unfolding as calculated for a $5 \times 5 \times 5$ supercell geometry of $SrTiO_3$, which is an exact periodic replica of the unit cell containing atoms at their relaxed classical positions. Examples of spectral functions obtained by supercell calculations on perturbed configurations exploring the harmonic (left) and anharmonic (right) potential-energy surfaces for $T = 300$ and 1200 K are shown in Fig. 2(b). The relevant computational details are provided in Sec. III.

III. COMPUTATIONAL DETAILS

All calculations were performed with the all-electron, full-potential, numeric-atomic orbital code FHI-AIMS [31] using density-functional theory (DFT) with the local-density approximation (LDA) for Si and DFT with the Perdew-Burke-Ernzerhof (PBE) functional for $SrTiO_3$. In the latter case, van der Waals interactions were included using the Tkatchenko-Scheffler method [56]. For both structures, light defaults were used for the numerical settings and for the basis set. With respect to Brillouin zone (BZ) integrations, $12 \times 12 \times 12$ (Si)/$5 \times 5 \times 5$ ($SrTiO_3$) $\boldsymbol{k}$ grids (in the primitive BZ) were used during the self-consistency cycle.

Table I summarizes the lattice constants and band gaps computed for static, cubic $SrTiO_3$ using different exchange-correlation functionals (LDA, PBE, PBE functional revised for solids (PBEsol) [58], and Heyd-Scuseria-Ernzerhof (HSE06) hybrid functional [59]), with and without van der Waals (vdW) interactions. Generally, we observe that vdW interactions stabilize the cubic structure, curing the typical underbinding observed with the PBE functional. All LDA and generalized gradient approximation (GGA) functionals severely underestimate the experimental band gap of 3.26 eV [36] by at least 1 eV, whereas HSE06 and HSE06-vdW yield static band gaps of 3.63 and 3.45 eV, respectively. The fact that PBE-vdW yields excellent agreement with respect to experimental lattice expansion data, validates our choice of the functional used for all stAVIC calculations on $SrTiO_3$.

Harmonic phonon properties were calculated using finite differences as implemented in the software package PHONOPY [60]. The computed phonon frequencies and normal-mode coordinates were employed to sample the harmonic phase space via *importance sampling Monte Carlo* [24] to evaluate the thermodynamic averages $\langle\cdot\rangle_T^{\text{ha-qm}}$ and $\langle\cdot\rangle_T^{\text{ha-cl}}$ using quantum-mechanical and classical statistics, respectively. Soft modes with imaginary phonon frequencies are

TABLE I. Lattice constant and band gap of cubic $SrTiO_3$ calculated within density-functional theory using the LDA, PBE, PBEsol, and HSE06 exchange-correlation (XC) functionals. Van der Waals (vdW) interactions are accounted for via the Tkatchenko-Scheffler method [56].

XC functional	Lattice constant (Å)	Bang gap (eV)
LDA	3.86	2.00
PBE	3.96	2.30
PBE-vdW	3.90	2.09
PBEsol	3.90	2.10
PBEsol-vdW	3.87	2.00
HSE06	3.91	3.63
HSE06-vdW	3.85	3.45
Expt. ($T = 140$ K)	3.90 [57]	3.26 [36]

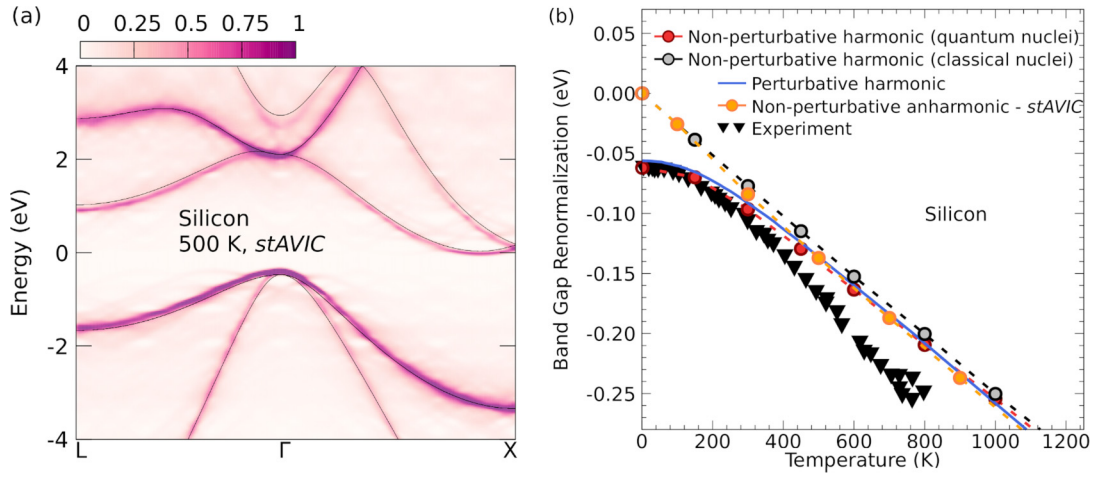

FIG. 3. (a) Thermodynamically averaged spectral function $\langle A_{\mathbf{k}}^{\boldsymbol{R}(t)}(E)\rangle_T$ of silicon along L-Γ-X (256 **k** points) for $T = 500$ K calculated with stAVIC using DFT-LDA and 30 uncorrelated geometries in a $6 \times 6 \times 6$ supercell containing 432 atoms. The band structure in static equilibrium is shown as black lines. (b) Vibronic renormalization of the band gap $\Delta\langle\epsilon_g\rangle_T = \langle\epsilon_g\rangle_T - \langle\epsilon_g\rangle_{0K}^{\text{ha-cl}}$ of silicon as function of temperature obtained via the stAVIC $\Delta\langle\epsilon_g\rangle_T^{\text{MD}}$ (orange) and via the nonperturbative harmonic approach: $\Delta\langle\epsilon_g\rangle_T^{\text{ha-cl}}$ (gray) and $\Delta\langle\epsilon_g\rangle_T^{\text{ha-qm}}$ (red). All calculations were performed using DFT-LDA and $6 \times 6 \times 6$ supercells containing 432 atoms. Perturbative harmonic calculations (blue, [13]) and experimental data (black, [64]) are shown as well.

"frozen in" in this harmonic approach (∼1% of all modes in the employed $SrTiO_3$ supercells).

Born-Oppenheimer aiMD simulations were carried out in the canonical ensemble (*NVT*) using a time step of 1 fs and the Bussi-Donadio-Parrinello thermostat [61]. Trajectories with a time length of 1.5–2.0 ps for Si and $SrTiO_3$ were used to thermally equilibrate the systems. An additional 1.0–2.0 ps for Si and $SrTiO_3$ of aiMD were simulated for the stAVIC evaluation. Thermal lattice expansion was calculated by computing the thermodynamic average of the stress tensor observed during an aiMD trajectory; subsequently, the structure was reoptimized under external pressure to obtain temperature-dependent geometries for which the stress tensor becomes negligible in the thermodynamic average [62]. As shown in Appendix A, a significant band gap opening is induced when considering thermal lattice expansion in $SrTiO_3$.

The band gaps at finite temperatures are obtained by averaging over 50 (Si) and 100 ($SrTiO_3$) configurations, which are selected from the already equilibrated aiMD trajectory in steps of 0.01 ps. For the aiMD, $6 \times 6 \times 6$ supercells with 432 atoms (Si) and $5 \times 5 \times 5$ supercells with 625 atoms ($SrTiO_3$) were used. Both the chosen number of configurations for the thermodynamic averaging and the chosen supercell sizes ensure a convergence of the temperature-dependent band gap within $\ll \pm 5\%$. We note that finite supercell size effects and symmetry breaking lead to the splitting of degenerate states, as observed for the triply degenerate valence band maximum of Si before [25,63]. In this case, we determine the energy change of the band as the mean renormalization of all originally degenerate bands [63]. For high temperatures ($T > 500\,K$) the large quasiparticle linewidths lead to a large spectral broadening, making the quasiparticle peaks of the band edges hard to distinguish. As a second check, band gaps were additionally determined by analyzing the thermodynamically averaged joint density of states [25], as discussed in Appendix C. For all investigated temperatures, the analysis of the joint density of states confirmed our stAVIC calculations. The temperature-dependent electron effective masses of $SrTiO_3$ were extracted from the calculated momentum-resolved spectral functions by performing parabolic fits of these spectral functions in the proximity of the conduction band minimum Γ along the corresponding high-symmetry paths connecting Γ-R and Γ-M.

Let us note that eventually, the computational cost is dominated by the sampling of the phase space, i.e., the *ab initio* MD in the stAVIC calculations. The numerical effort to perform the BZ unfolding and obtain spectral functions is comparable to a few self-consistency cycles.

IV. RESULTS

In this section we demonstrate the potential of our methodology in calculating full temperature-dependent band structures and band gaps that include anharmonic effects and all orders of vibronic coupling. As validation, we show that our approach reproduces harmonic data for Si, for which the perturbative Allen-Heine approach performs particularly well, and then we present temperature-dependent spectral functions, band gaps, and effective masses for cubic $SrTiO_3$.

A. stAVIC: Temperature-dependent band structure of Si

Figure 3(a) shows the momentum-resolved spectral function of Si along the high-symmetry path L-Γ-X at 500 K, as calculated using the stAVIC approach. For comparison purposes we also include the band structure of Si calculated for the unit cell with the nuclei at static equilibrium. The differences between the two plots reflect essentially the effect of vibronic coupling on the band structure. For example, identifying the positions of quasiparticle peaks of the spectral function reveals that the valence band top at Γ increases in energy by 73 meV, and the conduction band bottom at 0.83

Γ-X decreases in energy by 64 meV, leading to a total band gap renormalization of 137 meV.

Figure 3(b) shows the temperature dependence of the band gap renormalization $\Delta\langle\epsilon_g\rangle_T = \langle\epsilon_g\rangle_T - \langle\epsilon_g\rangle_{0K}^{\text{ha-cl}}$ of bulk Si. Our aiMD-based stAVIC calculations $\Delta\langle\epsilon_g\rangle_T^{\text{MD}}$ are in excellent agreement with reference data $\Delta\langle\epsilon_g^{\text{pt}}\rangle_T^{\text{ha-qm}}$ obtained with the perturbative, harmonic formalism [13] for $T \gg 400$ K. Discrepancies at lower temperatures are exclusively caused by quantum-nuclear effects not captured in aiMD. In Fig. 3(b), this is demonstrated by comparing nonperturbative, harmonic data obtained by evaluating Eq. (2) with Monte Carlo sampling [24,65] using classical $\Delta\langle\epsilon_g\rangle_T^{\text{ha-cl}}$ and quantum-mechanical $\Delta\langle\epsilon_g\rangle_T^{\text{ha-qm}}$ statistics. In both cases, anharmonic effects are thus neglected, while higher-order vibronic couplings are included via Eq. (5). The fact that the anharmonic $\Delta\langle\epsilon_g\rangle_T^{\text{MD}}$ and harmonic $\Delta\langle\epsilon_g\rangle_T^{\text{ha-cl}}$ approaches almost coincide in the classical limit proves that anharmonic effects are, indeed, negligible for silicon and that discrepancies with experiment at high T reflect the deficiencies of the LDA functional [27,63]. Similarly, higher-order vibronic couplings are negligible here, given that the nonperturbative $\Delta\langle\epsilon_g\rangle_T^{\text{ha-qm}}$ and perturbative $\Delta\langle\epsilon_g^{\text{pt}}\rangle_T^{\text{ha-qm}}$ data follow each other closely. Quantitatively, this is substantiated by the fact that our $\Delta\langle\epsilon_g\rangle_T^{\text{ha-qm}}$ calculations yield a quantum zero-point renormalization of 62 meV, in line with previous harmonic approaches (56–62 meV) [23–26] and with experimental values (62–64 meV) [66,67].

B. stAVIC: Temperature-dependent band structure of $SrTiO_3$

Unlike Si, AVICs are not negligible for many materials [21,22,29,30,68–70], as we demonstrate here for the prototypical perovskite $SrTiO_3$. At $T = 0$ K, this material exhibits a tetragonal $I4/mcm$ structure ($c/a = 0.998$), in which the individual tetrahedra are slightly tilted with respect to each other [71]. Above 105 K [72] and up to its melting point at 2300 K [36], $SrTiO_3$ exhibits a cubic $Pm3m$ structure, in which all tetrahedra appear to be aligned [see Fig. 4(a)]. This cubic structure does not correspond to a minimum but to a saddle point of the PES and thus features imaginary phonon frequencies. Even in the cubic lattice ($c/a = 1$), the tetrahedra favor a tilted arrangement in the static limit, corresponding to the minima in Fig. 4(a). Thermodynamic hopping between these wells results, on average, in an apparent alignment of the tetrahedra, in close analogy to other vibrationally stabilized materials [74–77]. Perturbative approaches cannot capture this complex dynamics that is commonly observed in perovskites [21,30,62]: If the saddle point with aligned tetrahedra is chosen as the static equilibrium $\boldsymbol{R}^{\text{eq}}$, phonon modes with imaginary frequencies have to be frozen in [30], and their coupling to the electronic structure is neglected. If one of the minima with tilted tetrahedra is chosen as $\boldsymbol{R}^{\text{eq}}$, both the harmonic approximation for the PES and the parabolic electron-phonon model become not only inaccurate but even qualitatively wrong at elevated temperatures, at which multiple minima are explored, as shown by the parabolic fits in Fig. 4(a). In other words, perturbative calculations require us to assume either (a) a tilted alignment at all temperatures or (b) that the modes responsible for the stabilization of the cubic polymorph above 105 K are insignificant. Neither of these assumptions is justified, and the breakdown of the harmonic, perturbative model has a direct impact on the thermodynamic properties of $SrTiO_3$.

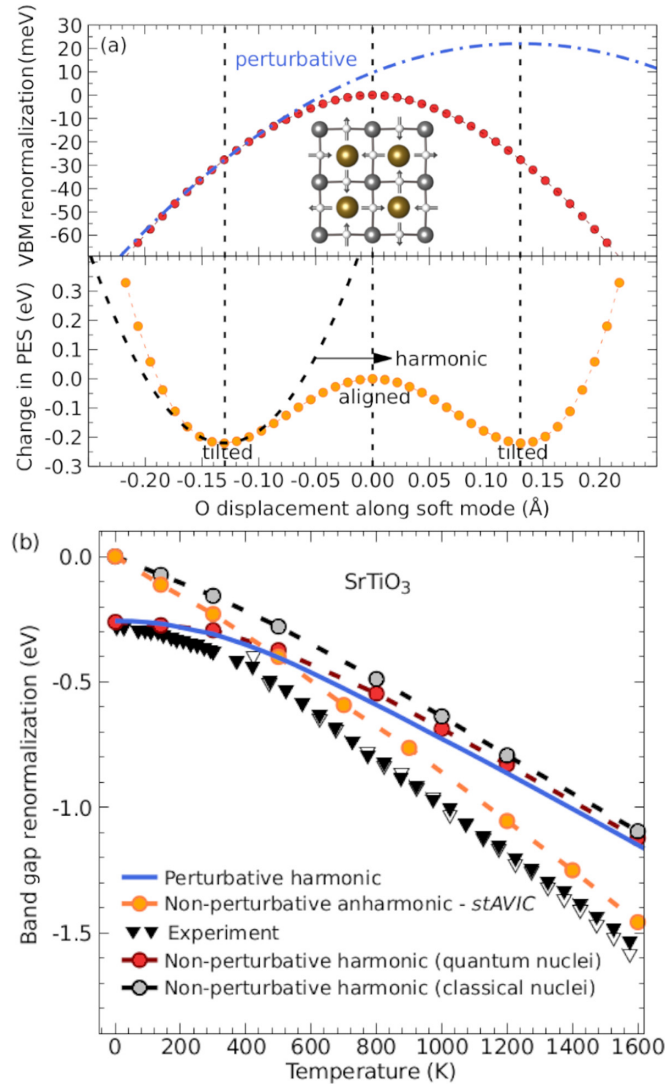

FIG. 4. (a) Energy of the valence band maximum (red) and PES (orange) of $SrTiO_3$ as a function of the displacement of atoms along the soft phonon mode at the R point. The direction of these displacements is shown as arrows in the planar ball-and-stick model of $SrTiO_3$. O, Ti, and Sr atoms are represented by white, gray, and brown spheres, respectively. Parabolic fits at the tilted minimum are shown in blue and black. (b) Band gap renormalization of cubic $SrTiO_3$ as a function of temperature calculated using DFT-PBE and $5 \times 5 \times 5$ supercells (625 atoms). Perturbative harmonic calculations $\Delta\langle\epsilon_g^{\text{pt}}\rangle_T^{\text{ha-qm}}$ using finite differences [73] are shown in blue; nonperturbative harmonic calculations $\Delta\langle\epsilon_g\rangle_T^{\text{ha-cl}}$ and $\Delta\langle\epsilon_g\rangle_T^{\text{ha-qm}}$ are in red and gray, and nonperturbative anharmonic stAVIC calculations $\Delta\langle\epsilon_g\rangle_T^{\text{MD}}$ are in orange. Long-range polar interactions are accounted for in all cases (see Appendix B). Triangles represent experimental data [36]; the respective band gap in the static limit (3.568 eV) was determined via linear regression [67] from the high $T > 800$ K data.

The temperature dependence of the band gap renormalization of $SrTiO_3$ is shown in Fig. 4(b). Examples of the

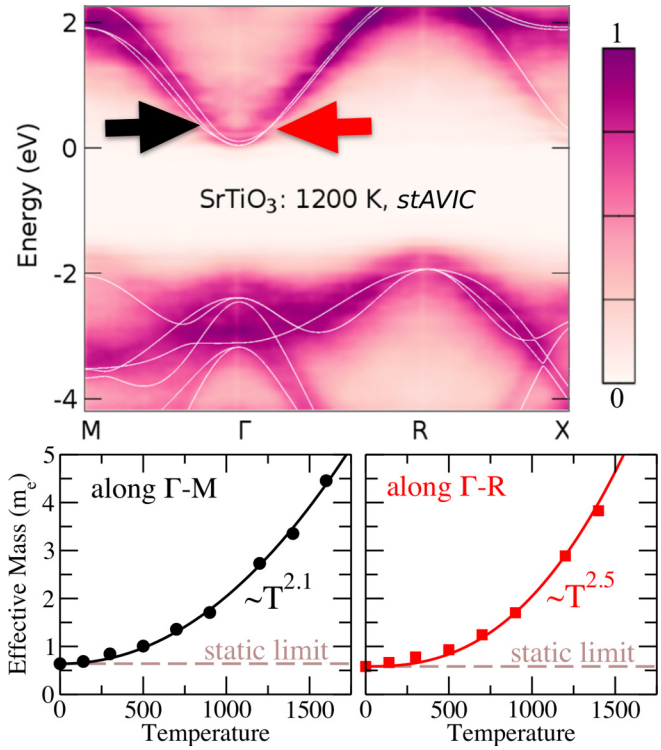

FIG. 5. Thermodynamically averaged spectral function $\langle A_{\mathbf{k}}^{\boldsymbol{R}(t)}(E)\rangle_T$ of cubic $SrTiO_3$ for $T = 1200\,\mathrm{K}$ calculated with stAVIC using DFT-PBE and 30 uncorrelated geometries in a $5 \times 5 \times 5$ supercell containing 625 atoms. The band structure in static equilibrium is shown as white lines. The extracted, temperature-dependent electron effective masses along Γ-*R* and Γ-*M* are shown below.

spectral functions calculated along Γ-*R* at 300 and 1200 K are shown in Fig. 2(b). Corrections [78] for long-range polar effects [79] that are not fully captured within the finite aiMD supercells are included. Thermal lattice expansion and the associated, non-negligible band gap opening of, e.g., 154 meV at 1000 K are also accounted for nonperturbatively. Details on the treatment of lattice expansion and polar effects on the band gap renormalization are given in Appendixes A and B, respectively. As discussed for Fig. 3(b), the fact that $\Delta\langle\epsilon_g\rangle_T^{\text{ha-cl}}$ and $\Delta\langle\epsilon_g\rangle_T^{\text{ha-qm}}$ become comparable for $T > 500\,\mathrm{K}$ implies that the use of classical aiMD is justified in this regime. In contrast to Si, distinct deviations between harmonic $\Delta\langle\epsilon_g\rangle_T^{\text{ha-cl}}$ and anharmonic $\Delta\langle\epsilon_g\rangle_T^{\text{MD}}$ data are observed for $SrTiO_3$, leading to an additional renormalization in stAVIC as large as 147 meV at 600 K and 260 meV at 1200 K. With respect to the perturbative, harmonic data, this corresponds to a remarkable increase of 18% and 27%, respectively. With respect to experiment [36], stAVIC improves the agreement significantly and quantitatively reproduces the measured high-temperature slope. This has substantial influence on the actual properties of $SrTiO_3$; for example, this band gap narrowing massively increases intrinsic charge carrier densities $n_c \propto \exp[-\langle\epsilon_g\rangle_T/(2k_BT)]$ by two orders of magnitude at 1000 K.

More insights can be obtained from the momentum-resolved spectral functions, e.g., by extracting the electron effective masses $m_e^*(T)$ along Γ-*R* and Γ-*M*, as done in Fig. 5. These particular effective masses have been the topic of debate [37,80] since *ab initio* calculations [81,82] of $SrTiO_3$ systematically underestimate measured values by a factor of 2 or more [82,83]. The stAVIC calculations reveal a large enhancement of $m_e^*(T)$ with T, confirming the important role of the nuclear motion suggested by experiments [37,80]. The strong temperature dependence $\propto T^{2.1-2.5}$ also substantiates the hypothesis [84] that $m_e^*(T)$ is responsible for the unusually large decrease in Hall mobility $\propto T^{-2.7}$ at high temperatures [85] that defies harmonic models yielding $\propto T^{-1.5}$ [84]. Certainly, this dictates further research along these lines to disentangle the influence of AVICs on, e.g., charge carrier densities, effective masses, and scattering mechanisms (lifetimes and linewidths), as well as on the interplay with polaronic [86] and quantum-nuclear effects at low T [47].

V. CONCLUSIONS

In this work, we have demonstrated a fully anharmonic, nonperturbative theory of the vibronic interactions in solids that overcomes the two main approximations (harmonic and electron-phonon coupling models) that limit the applicability of perturbative state-of-the-art formalisms [22,29,30]. The presented stAVIC methodology gives access to momentum-resolved electronic spectral functions and, in turn, to a plethora of other electronic properties [44]. As demonstrated for the perovskite $SrTiO_3$, accounting for AVICs is pivotal at elevated temperatures and/or in strongly anharmonic materials. stAVIC thus lends itself to aiding and guiding in silico materials design of high-temperature applications, e.g., for optical gas sensing in next-generation combustion chambers [38], solid oxide fuel cells [39,40], and thermoelectric waste-heat recovery devices [41,42], as well as hybrid photovoltaic cells operating under concentrated sunlight [43]. For all these applications, in which perovskites and also many other highly anharmonic materials play a substantial role, an accurate assessment of the temperature-dependent, momentum-resolved electronic structure is essential since the associated electronic properties such as band gaps and effective masses [87,88], as well as the anisotropic band structure corrugation [89], are critical for the material's performance.

All the electronic structure theory calculations produced in this project are available on the Novel Materials Discovery (NOMAD) repository [90].

ACKNOWLEDGMENTS

C.C. thanks H.-H. Kowalski, F. Knoop, and F. Bechstedt for fruitful discussions. This project was supported by TEC1p [the European Research Council (ERC) Horizon 2020 research and innovation program, Grant Agreement No. 740233], BigMax (the Max Planck Society's Research Network on Big-Data-Driven Materials-Science), and the NOMAD pillar of the FAIR-DI e.V. association.

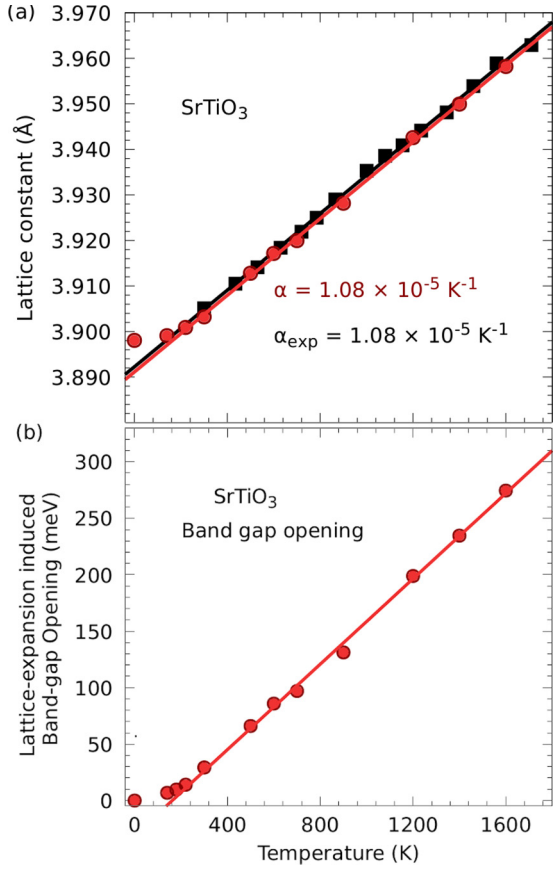

FIG. 6. (a) Calculated lattice constant of cubic $SrTiO_3$ as a function of temperature (red disks) versus experimental data from Ref. [91] (black squares). For each case the linear thermal expansion coefficient is indicated. The linear fits for $T > 300\,\mathrm{K}$ are guides to the eye. (b) Temperature-dependent renormalization of the band gap of cubic $SrTiO_3$ due to thermal lattice expansion. The linear fit for $T > 300\,\mathrm{K}$ is a guide to the eye.

APPENDIX A: THERMAL LATTICE EXPANSION OF $SrTiO_3$

The computed temperature dependence of the lattice constant of $SrTiO_3$, which is associated with its thermal expansion, was calculated by running aiMD in $6 \times 6 \times 6$ supercells containing 1080 atoms, thus taking anharmonic effects into account [62]. As shown in Fig. 6(a), we observe a linear increase of the lattice constant for $T > 200\,K$, i.e., for temperatures in which the cubic structure is, indeed, stable. This corresponds to a considerable linear thermal expansion coefficient of $\alpha_\mathrm{L} = \frac{1}{a(T)}\frac{\partial a(T)}{\partial T} \approx 1.1 \times 10^{-5}\ \mathrm{K}^{-1}$, which is in excellent agreement with the corresponding experimental value extracted from the measured data reported in Ref. [91]. The lattice expansion induces a significant opening of the band gap as the temperature increases, for example, 154 meV at 1000 K, as shown in Fig. 6(b). This effect is accounted for in all calculations of the band gap renormalization of $SrTiO_3$ discussed in the main text. Let us note that thermal lattice expansion has not been accounted for in the stAVIC calculations for the band gap renormalization of Si to allow for a consistent comparison to literature data. Furthermore, our calculations reveal that this effect is negligible in Si even at high temperatures, resulting, for example, in a band gap opening of 13 meV at 1100 K.

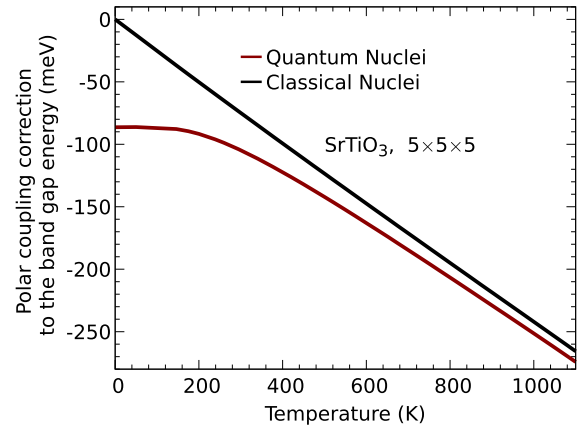

FIG. 7. Fröhlich polar coupling correction [Eq. (B1)] to the band gap of $SrTiO_3$ for a $5 \times 5 \times 5$ supercell as a function of temperature using quantum (red) and classical (black) occupation numbers.

APPENDIX B: POLAR FRÖHLICH COUPLING

In polar materials, there is an additional contribution to the energy level renormalization stemming from long-range Fröhlich coupling [78,79,92,93] that is not fully captured in the limited supercells used in aiMD. We account for the missing portion of these effects via the following analytic correction for the adiabatic case [46,78,79]:

$$\left\langle \Delta\epsilon_l^{\mathrm{Fr}\backslash\mathrm{HA}} \right\rangle_T = \frac{2}{\pi}\alpha\hbar\omega_\mathrm{LO}\tan^{-1}\left(\frac{q_\mathrm{F}}{q_\mathrm{LO}}\right)[2n_T + 1], \qquad \text{(B1)}$$

which can be obtained by integrating Eq. (B3) of Ref. [46] up to the truncation parameter q_F defined below. In Eq. (B1), the strength of the polar coupling is characterized by the

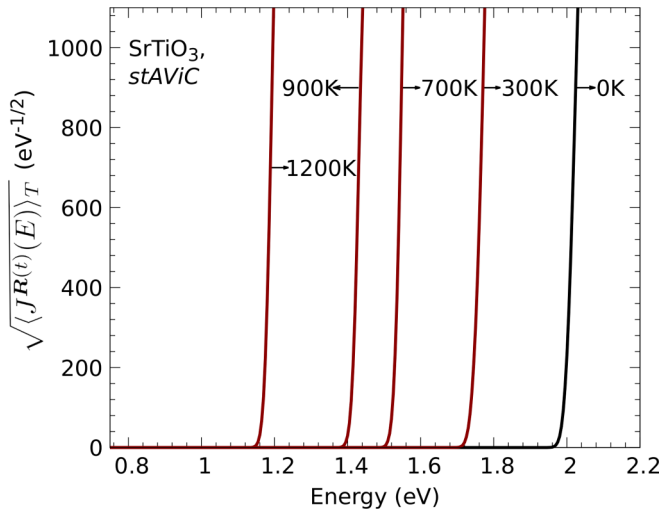

FIG. 8. Temperature-dependent square-root joint density of states of $SrTiO_3$ calculated using stAVIC and $5 \times 5 \times 5$ supercells containing 625 atoms. The black line represents the square-root joint density of states evaluated with atoms at static equilibrium.

dimensionless polaron constant given by [94]

$$\alpha = \frac{e^2}{4\pi\epsilon_0}\frac{1}{\hbar}\left(\frac{1}{\kappa_\infty}-\frac{1}{\kappa_0}\right)\left(\frac{m^*}{2\hbar\omega_{\mathrm{LO}}}\right)^{1/2}, \tag{B2}$$

where m^* is the effective mass of the carrier, ω_{LO} is the frequency of the LO phonon, and κ_∞, κ_0 are the high-frequency dielectric constant and static permittivity, respectively. The quantity $n_T = [\exp(\hbar\omega_{\mathrm{LO}}/k_{\mathrm{B}}T)-1]^{-1}$ is the Bose-Einstein occupation factor of the LO mode, and q_{LO} is defined as $\sqrt{2m^*(\omega_{\mathrm{LO}}+\omega)/\hbar}$, where $\hbar\omega$ is the energy of the state. The radius of integration q_{F} is used as a truncation parameter to avoid a double counting of the Fröhlich interactions already accounted for in the aiMD supercell. For our calculations we take q_{F} equal to the radius of the Debye sphere, i.e., to the sphere with the same volume as the Brillouin zone of the employed $5\times5\times5$ supercell. In order to evaluate Eq. (B1) we set the LO phonon energy to $\hbar\omega_{\mathrm{LO}} = 59$ meV [95], the light-electron and light-hole effective masses along $\mathrm{R}\rightarrow\Gamma$ to $m_e = 0.537$ and $m_h = 0.944$ [81], and the high-frequency dielectric constant to $\kappa_\infty = 5.5$ [96]. The static permittivity of $SrTiO_3$ exhibits a large variation with temperature, and therefore, we extract the temperature dependence of κ_0 from Ref. [95]. Our calculations of the temperature-dependent polar coupling correction to the band gap of $SrTiO_3$ for a $5\times5\times5$ supercell are shown in Fig. 7. For classical nuclei (black), the square bracket in Eq. (B1) is replaced by its classical limit without zero-point vibrations, which results in a correction that varies linearly from 0 meV at $T = 0$ K to -265 meV at $T = 1100$ K.

APPENDIX C: EVALUATION OF BAND GAPS VIA THE JOINT DENSITY OF STATES

For the calculation of the joint density of states at each aiMD step $\boldsymbol{R}(t)$ we consider the following relationship:

$$J^{\boldsymbol{R}(t)}(E) = \sum_{c\mathbf{k}_c,u\mathbf{k}_u}\delta\left(\epsilon^{\boldsymbol{R}(t)}_{c\mathbf{k}_c}-\epsilon^{\boldsymbol{R}(t)}_{u\mathbf{k}_u}-E\right), \tag{C1}$$

where the summation runs over all conduction and valence state indices $c\mathbf{k}_c$ and $u\mathbf{k}_u$. In order to determine the temperature dependence of the band gap we consider the energy offset between the thermodynamically averaged square-root joint density of states for temperatures T and 0 K, i.e., the energy offset between $\sqrt{\langle J^{\boldsymbol{R}(t)}(E)\rangle_T}$ (red lines in Fig. 8) and $\sqrt{\langle J^{\boldsymbol{R}(t)}(E)\rangle_{0\mathrm{K}}}$ (black line in Fig. 8).

[1] P. Blaha, K. Schwarz, F. Tran, R. Laskowski, G. K. H. Madsen, and L. D. Marks, J. Chem. Phys. **152**, 074101 (2020).
[2] D. Golze, M. Dvorak, and P. Rinke, Front. Chem. **7**, 6158 (2019).
[3] W. Chen and A. Pasquarello, Phys. Rev. B **86**, 035134 (2012).
[4] P. B. Allen and V. Heine, J. Phys. C **9**, 2305 (1976).
[5] A. Marini, Phys. Rev. Lett. **101**, 106405 (2008).
[6] F. Giustino, S. G. Louie, and M. L. Cohen, Phys. Rev. Lett. **105**, 265501 (2010).
[7] E. Cannuccia and A. Marini, Phys. Rev. Lett. **107**, 255501 (2011).
[8] E. Cannuccia and A. Marini, Eur. Phys. J. B **85**, 320 (2012).
[9] G. Antonius, S. Poncé, P. Boulanger, M. Côté, and X. Gonze, Phys. Rev. Lett. **112**, 215501 (2014).
[10] S. Poncé, G. Antonius, Y. Gillet, P. Boulanger, J. Laflamme Janssen, A. Marini, M. Côté, and X. Gonze, Phys. Rev. B **90**, 214304 (2014).
[11] S. Poncé, G. Antonius, P. Boulanger, E. Cannuccia, A. Marini, M. Côté, and X. Gonze, Comput. Mater. Sci. **83**, 341 (2014).
[12] H. Kawai, K. Yamashita, E. Cannuccia, and A. Marini, Phys. Rev. B **89**, 085202 (2014).
[13] S. Poncé, Y. Gillet, J. Laflamme Janssen, A. Marini, M. Verstraete, and X. Gonze, J. Chem. Phys. **143**, 102813 (2015).
[14] A. Molina-Sánchez, M. Palummo, A. Marini, and L. Wirtz, Phys. Rev. B **93**, 155435 (2016).
[15] J.-J. Zhou and M. Bernardi, Phys. Rev. B **94**, 201201(R) (2016).
[16] J. Menéndez, M. Noël, J. C. Zwinkels, and D. J. Lockwood, Phys. Rev. B **96**, 121201(R) (2017).
[17] S. Poncé, E. R. Margine, and F. Giustino, Phys. Rev. B **97**, 121201(R) (2018).
[18] J. D. Querales-Flores, J. Cao, S. Fahy, and I. Savić, Phys. Rev. Mater. **3**, 055405 (2019).
[19] J.-M. Lihm and C.-H. Park, Phys. Rev. B **101**, 121102(R) (2020).
[20] B. Monserrat, N. D. Drummond, and R. J. Needs, Phys. Rev. B **87**, 144302(R) (2013).
[21] C. E. Patrick, K. W. Jacobsen, and K. S. Thygesen, Phys. Rev. B **92**, 201205 (2015).
[22] G. Antonius, S. Poncé, E. Lantagne-Hurtubise, G. Auclair, X. Gonze, and M. Côté, Phys. Rev. B **92**, 085137 (2015).
[23] B. Monserrat and R. J. Needs, Phys. Rev. B **89**, 214304 (2014).
[24] M. Zacharias, C. E. Patrick, and F. Giustino, Phys. Rev. Lett. **115**, 177401 (2015).
[25] M. Zacharias and F. Giustino, Phys. Rev. B **94**, 075125 (2016).
[26] B. Monserrat, Phys. Rev. B **93**, 014302 (2016).
[27] B. Monserrat, Phys. Rev. B **93**, 100301(R) (2016).
[28] N. Shulumba, Z. Raza, O. Hellman, E. Janzén, I. A. Abrikosov, and M. Odén, Phys. Rev. B **94**, 104305 (2016).
[29] B. Monserrat, E. A. Engel, and R. J. Needs, Phys. Rev. B **92**, 140302(R) (2015).
[30] W. A. Saidi, S. Poncé, and B. Monserrat, J. Phys. Chem. Lett. **7**, 5247 (2016).
[31] V. Blum, R. Gehrke, F. Hanke, P. Havu, V. Havu, X. Ren, K. Reuter, and M. Scheffler, Comput. Phys. Commun. **180**, 2175 (2009).
[32] G. Rupprecht, R. O. Bell, and B. D. Silverman, Phys. Rev. **123**, 97 (1961).

[33] R. A. Cowley, Phys. Rev. Lett. **9**, 159 (1962).
[34] P. M. Woodward, Acta Crystallogr., Sect. B **53**, 32 (1997).
[35] J.-H. Lee, N. C. Bristowe, J. H. Lee, S.-H. Lee, P. D. Bristowe, A. K. Cheetham, and H. M. Jang, Chem. Mater. **28**, 4259 (2016).
[36] D. J. Kok, K. Irmscher, M. Naumann, C. Guguschev, Z. Galazka, and R. Uecker, Phys. Status Solidi A **212**, 1880 (2015).
[37] S. J. Allen, B. Jalan, S. B. Lee, D. G. Ouellette, G. Khalsa, J. Jaroszynski, S. Stemmer, and A. H. MacDonald, Phys. Rev. B **88**, 045114 (2013).
[38] A. M. Schultz, T. D. Brown, and P. R. Ohodnicki, Jr., J. Phys. Chem. C **119**, 6211 (2015).
[39] O. Marina, Solid State Ionics **149**, 21 (2002).
[40] S. J. Skinner, Int. J. Inorg. Mater. **3**, 113 (2001).
[41] H. Ohta, S. Kim, Y. Mune, T. Mizoguchi, K. Nomura, S. Ohta, T. Nomura, Y. Nakanishi, Y. Ikuhara, M. Hirano, H. Hosono, and K. Koumoto, Nat. Mater. **6**, 129 (2007).
[42] J. W. Fergus, J. Eur. Ceram. Soc. **32**, 525 (2012).
[43] G. C. Brunauer, B. Rotter, G. Walch, E. Esmaeili, A. K. Opitz, K. Ponweiser, J. Summhammer, and J. Fleig, Adv. Funct. Mater. **26**, 120 (2016).
[44] F. Giustino, Rev. Mod. Phys. **89**, 015003 (2017).
[45] B. Monserrat, J. Phys.: Condens. Matter **30**, 083001 (2018).
[46] M. Zacharias and F. Giustino, Phys. Rev. Res. **2**, 013357 (2020).
[47] R. Ramírez, C. P. Herrero, and E. R. Hernández, Phys. Rev. B **73**, 245202 (2006).
[48] A. Franceschetti, Phys. Rev. B **76**, 161301(R) (2007).
[49] T. B. Boykin and G. Klimeck, Phys. Rev. B **71**, 115215 (2005).
[50] P. B. Allen, T. Berlijn, D. A. Casavant, and J. M. Soler, Phys. Rev. B **87**, 085322 (2013).
[51] V. Popescu and A. Zunger, Phys. Rev. B **85**, 085201 (2012).
[52] P. V. C. Medeiros, S. Stafström, and J. Björk, Phys. Rev. B **89**, 041407(R) (2014).
[53] F. Bassani and G. Pastori Parravicini, *Electronic States and Optical Transition in Solids* (Pergamon, Oxford, 1975).
[54] W. Ku, T. Berlijn, and C.-C. Lee, Phys. Rev. Lett. **104**, 216401 (2010).
[55] C.-C. Lee, Y.-T. Yukiko, and O. Taisuke, J. Phys.: Condens. Matter **25**, 345501 (2013).
[56] A. Tkatchenko and M. Scheffler, Phys. Rev. Lett. **102**, 073005 (2009).
[57] F. W. Lytle, J. Appl. Phys. **35**, 2212 (1964).
[58] J. P. Perdew, A. Ruzsinszky, G. I. Csonka, O. A. Vydrov, G. E. Scuseria, L. A. Constantin, X. Zhou, and K. Burke, Phys. Rev. Lett. **102**, 039902(E) (2009).
[59] A. V. Krukau, O. A. Vydrov, A. F. Izmaylov, and G. E. Scuseria, J. Chem. Phys. **125**, 224106 (2006).
[60] A. Togo and I. Tanaka, Scr. Mater. **108**, 1 (2015).
[61] G. Bussi, D. Donadio, and M. Parrinello, J. Chem. Phys. **126**, 014101 (2007).
[62] A. van Roekeghem, J. Carrete, C. Oses, S. Curtarolo, and N. Mingo, Phys. Rev. X **6**, 041061 (2016).
[63] F. Karsai, M. Engel, G. Kresse, and E. Flage-Larsen, New J. Phys. **20**, 123008 (2018).
[64] V. Alex, S. Finkbeiner, and J. Weber, J. Appl. Phys. **79**, 6943 (1996).
[65] C. E. Patrick and F. Giustino, Nat. Commun. **4**, 2006 (2013).
[66] M. Cardona, Solid State Commun. **133**, 3 (2005).
[67] M. Cardona, Phys. Status Solidi A **188**, 1209 (2001).
[68] W. Lai, Y. Wang, D. T. Morelli, and X. Lu, Adv. Funct. Mater. **25**, 3648 (2015).
[69] T. Tadano and S. Tsuneyuki, Phys. Rev. Lett. **120**, 105901 (2018).
[70] M. Asher, D. Angerer, R. Korobko, Y. D. Posner, D. A. Egger, and O. Yaffe, Adv. Mater. **32**, 1908028 (2020).
[71] R. Loetzsch, A. Lübcke, I. Uschmann, E. Förster, V. Große, M. Thuerk, T. Koettig, F. Schmidl, and P. Seidel, Appl. Phys. Lett. **96**, 071901 (2010).
[72] P. K. Gogoi and D. Schmidt, Phys. Rev. B **93**, 075204 (2016).
[73] R. B. Capaz, C. D. Spataru, P. Tangney, M. L. Cohen, and S. G. Louie, Phys. Rev. Lett. **94**, 036801 (2005).
[74] S. Fabris, A. T. Paxton, and M. W. Finnis, Phys. Rev. B **63**, 094101 (2001).
[75] M. Sternik and K. Parlinski, J. Chem. Phys. **123**, 204708 (2005).
[76] I. Errea, B. Rousseau, and A. Bergara, Phys. Rev. Lett. **106**, 165501 (2011).
[77] C. Carbogno, C. G. Levi, C. G. Van de Walle, and M. Scheffler, Phys. Rev. B **90**, 144109 (2014).
[78] J. P. Nery and P. B. Allen, Phys. Rev. B **94**, 115135 (2016).
[79] H. Y. Fan, Phys. Rev. **82**, 900 (1951).
[80] J. L. M. van Mechelen, D. van der Marel, C. Grimaldi, A. B. Kuzmenko, N. P. Armitage, N. Reyren, H. Hagemann, and I. I. Mazin, Phys. Rev. Lett. **100**, 226403 (2008).
[81] M. Marques, L. K. Teles, V. Anjos, L. M. R. Scolfaro, J. R. Leite, V. N. Freire, G. A. Farias, and E. F. da Silva, Appl. Phys. Lett. **82**, 3074 (2003).
[82] A. Janotti, D. Steiauf, and C. G. Van de Walle, Phys. Rev. B **84**, 201304(R) (2011).
[83] M. Ahrens, R. Merkle, B. Rahmati, and J. Maier, Phys. B **393**, 239 (2007).
[84] H. P. R. Frederikse, W. R. Thurber, and W. R. Hosler, Phys. Rev. **134**, A442 (1964).
[85] O. N. Tufte and P. W. Chapman, Phys. Rev. **155**, 796 (1967).
[86] W. H. Sio, C. Verdi, S. Poncé, and F. Giustino, Phys. Rev. B **99**, 235139 (2019).
[87] Z. Huo, S.-H. Wei, and W.-J. Yin, J. Phys. D **51**, 474003 (2018).
[88] Y. Pei, A. D. LaLonde, H. Wang, and G. J. Snyder, Energy Environ. Sci. **5**, 7963 (2012).
[89] X. Chen, D. Parker, and D. J. Singh, Sci. Rep. **3**, 3168 (2013).
[90] http://doi.org/10.17172/NOMAD/2020.03.18-1.
[91] D. de Ligny and P. Richet, Phys. Rev. B **53**, 3013 (1996).
[92] C. Verdi and F. Giustino, Phys. Rev. Lett. **115**, 176401 (2015).
[93] J. Sjakste, N. Vast, M. Calandra, and F. Mauri, Phys. Rev. B **92**, 054307 (2015).
[94] G. D. Mahan, *Many-Particle Physics* (Plenum, New York, 1990), pp. 34, 438.
[95] J. L. Servoin, Y. Luspin, and F. Gervais, Phys. Rev. B **22**, 5501 (1980).
[96] R. A. Cowley, Phys. Rev. **134**, A981 (1964).